Solidification and Weldability of Nb-Bearing Superalloys

The relation between alloy composition, solidification behavior, microstructural development and solidification cracking susceptibility is established for a wide range of experimental alloys

BY J. N. DUPONT, C. V. ROBINO AND A. R. MARDER

ABSTRACT. The solidification and weldability of experimental superalloys containing systematic variations in Fe, Nb, Si and C were studied using differential thermal analysis (DTA), microstructural characterization techniques and Varestraint testing. Microstructural evolution during solidification of DTA samples and gas tungsten arc welds generally occurred by a three-step solidification process. Solidification initiated by a primary $L \rightarrow \gamma$ reaction, which enriches the interdendritic liquid in Nb and C until a eutectic-type $L \rightarrow (\gamma + NbC)$ reaction occurs over a rather broad temperature range. Solidification terminated by a second eutectic-type reaction, $L \rightarrow (\gamma +$ Lave), which occurred over a narrow temperature range. Carbon additions increased the start temperature of the $L \rightarrow (\gamma + NbC)$ reaction and induced a concomitant decrease in the temperature interval of the primary $L \rightarrow \gamma$ stage of solidification. As a result, carbon additions often promoted a significant improvement in solidification cracking resistance. The results from solidification studies are combined with detailed examinations of microstructural morphologies in fusion zone solidification cracks to propose a microstructure morphology classification scheme. The classification scheme provides a phenomenological explanation of the relation between alloy composition, solidification temperature range, microstructural morphology and cracking propensity. This interpretation also leads to an improved correlation between the solidification temperature range and fusion zone cracking susceptibility.

J. N. DUPONT and A. R. MARDER are with Lehigh University, Bethlehem, Pa. C. V. ROBINO is with Sandia National Laboratories, Albuquerque, N.Mex.

Introduction

Solidification Cracking

The formation of cracks during solidification can occur in ingots, castings and welds. The phenomenon has been investigated for quite some time and the general features are understood in a qualitative sense (Ref. 1). Work is also in progress to quantitatively determine conditions that lead to solidification cracking (Refs. 2, 3). In general, cracks can form in certain alloy systems during the terminal stages of solidification when a liquid film is distributed along grain boundaries and interdendritic regions. At this stage, shrinkage strains across the partially solidified boundaries can become appreciable. If the terminal liquid is distributed along the boundaries as a continuous film, the strains cannot be accommodated and the boundaries separate to form a crack. In terms of material factors, the solidification temperature range and morphology of the interfacial liquid that exists at the terminal stages of solidification are primary factors that control solidification cracking susceptibility. Solute redistribution plays an important role in solidification cracking as it affects the solidification temperature range and amount of terminal liquid. The effect of the solidification temperature range can be understood in simplified terms by considering its influence on the size of the solid + liquid (mushy) zone.

During welding, the mushy region trails behind the liquid weld pool. It is this mushy region that is susceptible to cracking under the influence of restraint. Assuming dendrite tip undercooling is negligible, the interface between the liquid weld pool and mushy zone (*i.e.*, start of the mushy zone) is located where the actual temperature intersects the liquidus temperature of the alloy. Similarly, the interface between the mushy zone and completely solidified weld (*i.e.*, end of the mushy zone) is positioned where the actual temperature intersects the terminal solidus temperature of the alloy. For a fixed temperature gradient in the mushy zone (constant processing parameters), composition variations that promote low-temperature eutectic-type reactions at the terminal stages of solidification will widen the solidification temperature range and generally aggravate cracking tendency by expanding the crack-susceptible mushy zone. The actual distance a solidification crack propagates through the mushy zone depends on the distribution of terminal liquid, which exists near the end of the solid + liquid region (Ref. 1). The distribution of liquid near the end of the mushy zone is, in turn, controlled by the amount of terminal liquid and

KEY WORDS

DTA
Hot Cracking
Solidification
Superalloys
Varestraint Testing
Weldability

Table 1 — Alloy Compositions

Alloy	Fe	Ni	Cr	Nb	Si	C	P	S
1	10.49	68.53	18.90	1.93	0.08	0.017	0.004	0.003
1.5	10.75	67.95	19.21	2.00	0.03	0.052	0.004	0.003
2	11.12	68.20	19.12	1.95	0.06	0.132	0.004	0.002
3	10.70	68.11	19.02	1.82	0.38	0.010	0.004	0.003
3.5	10.39	66.80	19.29	1.94	0.41	0.075	0.004	0.003
4	10.72	67.60	19.08	1.91	0.40	0.155	0.004	0.001
5	10.84	65.79	18.98	5.17	0.05	0.013	0.005	0.010
6	10.88	65.22	18.89	4.87	0.08	0.161	0.005	0.007
7	10.70	65.53	19.30	4.86	0.52	0.010	0.005	0.009
7.5	10.82	63.93	18.54	4.92	0.46	0.081	0.005	0.004
8	10.80	64.96	18.90	4.72	0.52	0.170	0.005	0.007
Ni-1	7.71	55.03	18.23	17.79	1.03	0.08	ND	ND
9	46.03	33.56	19.31	1.66	0.10	0.003	0.006	0.003
10	46.69	32.80	19.70	1.66	0.01	0.108	0.006	0.002
11	45.38	32.80	19.53	1.77	0.57	0.004	0.006	0.002
11.5	47.38	31.05	19.64	1.84	0.67	0.116	0.006	0.001
12	45.28	32.39	19.89	1.93	0.61	0.079	0.006	0.002
13	44.55	31.24	19.63	4.42	0.02	0.015	0.007	0.003
14	44.05	31.93	19.52	4.51	0.08	0.210	0.006	0.002
15	45.40	30.03	19.54	4.88	0.66	0.010	0.007	0.003
16	44.47	30.89	19.45	4.77	0.64	0.216	0.006	0.002

ND = Not determined. All values in wt-%.

solid/liquid surface tension. When the amount of terminal liquid is moderate, between approximately 1 to 10 vol-% (Ref. 4), and/or the surface tension is low, the liquid tends to wet the boundary and forms a continuous film. This type of morphology is most detrimental as it interferes with the formation of solid/solid boundaries, thus reducing the ability of the material to accommodate shrinkage strains. In contrast, a small amount of terminal liquid, generally less than approximately 1 vol-% (Ref. 4), which exhibits a high surface tension with the solid, will often exist as isolated globules and promote solid/solid bridging, thereby reducing cracking tendency. When the amount of terminal liquid is high, (greater than approximately 10 vol-%), it can often flow into the cracks and provide a "crack healing" effect (Refs. 4, 5). For a given alloy system, the solidification temperature range and amount of terminal liquid are controlled primarily by composition (processing parameters become important under high cooling rate conditions, where dendrite tip undercooling can be significant [Ref. 6]). Thus, many studies have been aimed at establishing the relation between solidification cracking susceptibility and alloy composition (Refs. 7–9).

Nb-Bearing Superalloys

Niobium-strengthened superalloys are used extensively in applications requiring high-temperature strength and resistance to oxidation. Commercial examples include alloys IN625, IN706, IN718, IN903, IN909 and Thermo-Span. These alloys are often used for components that are fabricated by fusion welding. Therefore, it is important to establish the relation between alloy composition and cracking tendency to avoid fusion zone cracking when these materials are used in critical applications. Previous studies conducted on commercial Nb-bearing superalloys (Refs. 7, 8, 10–12) have shown that minor variations in Nb, Si and C have a strong influence on the solidification temperature range, type and amount of secondary phases that form during the terminal stages of solidification and resultant solidification cracking susceptibility. In general, two types of eutectic-type constituents, γ/NbC and γ/Laves, are known to form as the weld metal solidifies. The γ/Laves constituent is most deleterious in terms of hot cracking as it forms at a lower temperature and thus expands the solidification temperature range. These alloys are also often joined to iron-based alloys such as carbon steels and stainless steels (Refs. 10, 13–15). In these applications, the fusion zone composition can become significantly enriched in Fe and C due to dilution effects, and this composition modification can significantly alter the solidification behavior and associated cracking tendency. For example, Patterson and Milewski evaluated the hot cracking susceptibility of dissimilar metal welds between 304L and IN625 (Ref. 14). The results of that work showed that the diluted fusion zones were more susceptible to cracking than either of the base materials. Subsequent work by Cieslak (Ref. 15) showed that the γ/Laves constituent forms in the fusion zone of this dissimilar alloy combination. Robitz (Ref. 13) evaluated the solidification cracking of IN625 claddings on C steel and found that Nb, Si, C and Fe all increased cracking susceptibility, although no detailed results were reported. DuPont (Ref. 10) showed that solidification cracking in IN625 weld cladding (deposited on C steel) was promoted by formation of the γ/Laves constituent. Despite the industrial importance of these superalloys and the need to minimize solidification cracking, no general model has been developed for predicting the relationship between alloy composition, solidification behavior (*e.g.*, solidification temperature range and amount of γ/NbC and γ/Laves) and resultant weldability. In separate articles, we reported on the development of a solidification model that can be used to predict the solidification temperature range and amounts of γ/NbC and γ/Laves constituents as a function of alloy composition (Refs. 16, 17). In this article, the link between solidification behavior and weldability is discussed for a wide range of experimental alloy compositions.

Experimental Procedure

Experimental Alloy Compositions

A four-factor, two-level set of experimental alloys was designed to simulate commercial compositions of interest to this study. The alloy compositions are summarized in Table 1. The alloys exhibit factorial variations in Fe (in exchange for Ni), Nb, Si and C at two levels. The high- and low-target levels of Nb, Si and C are set as follows (all values in wt-%): $2 < Nb < 5$, $0.02 < C < 0.15$ and $0.10 < Si < 0.60$. These limits were chosen to represent low and high composition values of

wrought alloys and filler metals as well as composition limits that can arise in fusion welds made between nickel-based alloys and carbon steels. The nominal Cr content was selected at 20 wt-%, which is typically used in many commercial alloys for good corrosion resistance. Several additional alloys with intermediate C contents (Alloys 1.5, 3.5, 7.5 and 11.5) were also investigated. The alloys were prepared at Sandia National Laboratories by investment casting. All samples were melted and poured in vacuum to produce six bars of each composition with approximate dimensions of 170 x 25 x 6.3 mm. A high-Nb alloy (Ni-1) was also added for supplemental differential thermal analysis measurements. Small cast buttons of this alloy were produced from high-purity powders (> 99.99 wt-%) by gas tungsten arc melting.

Differential Thermal Analysis

Differential thermal analysis (DTA) was conducted on a Netzsch STA 409 differential thermal analyzer using 500- to 550-mg samples. The DTA system was calibrated within 2°C of the melting point of pure Ni. Samples were melted and solidified under flowing argon in alumina crucibles using pure Ni as the reference material. The liquidus temperatures were determined by heating samples slowly at a rate of 5°C/min to approximately 10°C above their liquidus temperature. The samples were then solidified at a relatively fast cooling rate of 20°C/min to determine temperatures of eutectic-type reactions that occur under nonequilibrium solidification conditions. Reaction temperatures were taken as deviations from the local baseline. All reported reaction temperatures are an average from at least three tests, and the order of testing was randomized.

Varestraint Testing

The solidification cracking susceptibility of each alloy was evaluated using the Varestraint test (Refs. 18, 19). The as-cast samples were machined to typical subsize Varestraint specimens (165 x 25 x 3.2 mm). The welds were produced under the following parameters: 95 A, 10 V (2.5 mm arc length), and 3.3 mm/s travel speed with high-purity argon shielding. A 3.2-mm-diameter W-2ThO_2 electrode was used with a 60-deg tip angle. In order to acquire adequate statistics, three tests were conducted on each alloy at an augmented strain of 2.5% to simulate highly restrained welds. The maximum crack length (MCL) was used as the indicator of cracking susceptibility and was measured using a light optical microscope at 100X magnification. The level of 2.5% augmented strain was selected on the basis of a large number of tests at varying strain levels (conducted using essentially identical testing equipment, welding conditions and weld sizes) on a range of alloys with similar solidification characteristics and solidification microstructure (Refs. 8, 20, 26). These results have shown that for these test conditions, for alloys that solidify over similar temperature ranges and which exhibit MCL values spanning the range observed in the current study, the

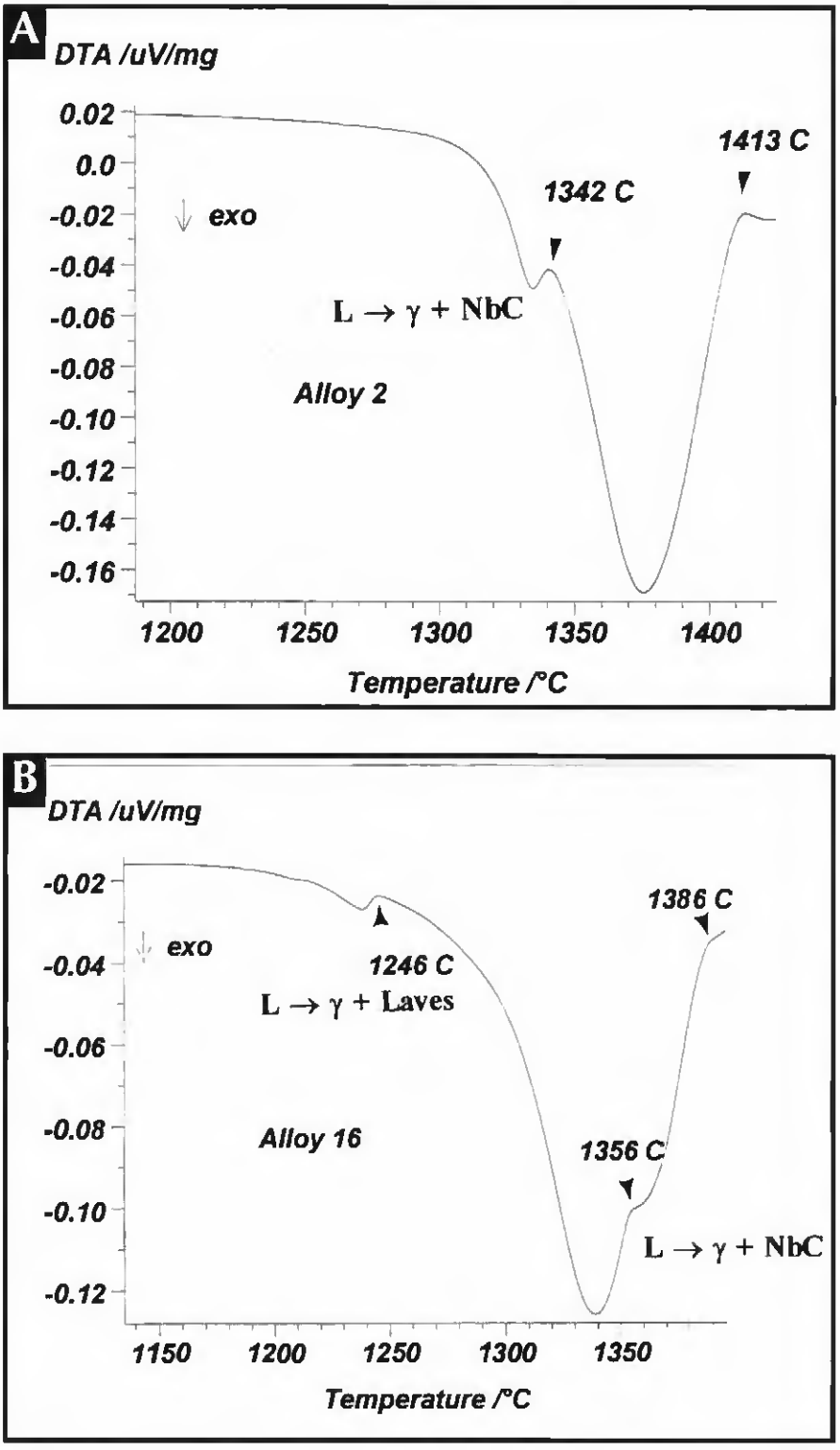

Fig. 1 — Typical DTA cooling scans. A — Alloy 2; B — Alloy 16.

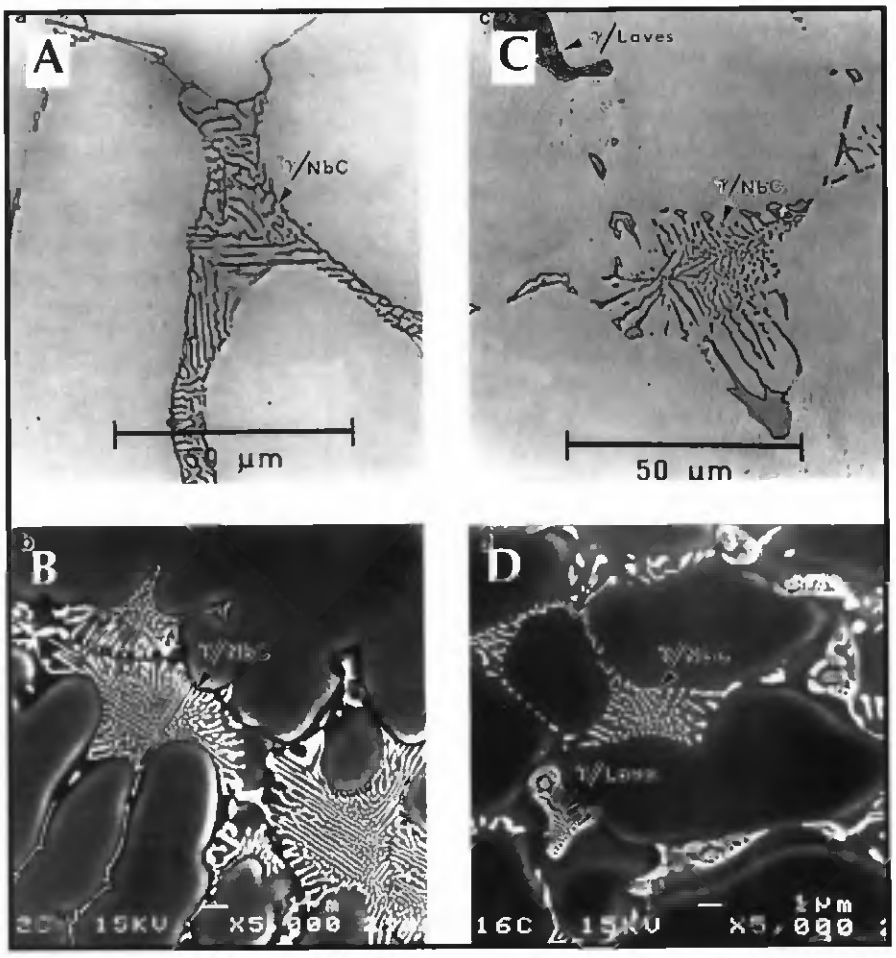

Fig. 2 — Microstructures of DTA samples and GTA welds for Alloy 2 and Alloy 16. A — Alloy 2 DTA sample; B — Alloy 2 weld; C — Alloy 16 DTA sample; D — Alloy 16 weld.

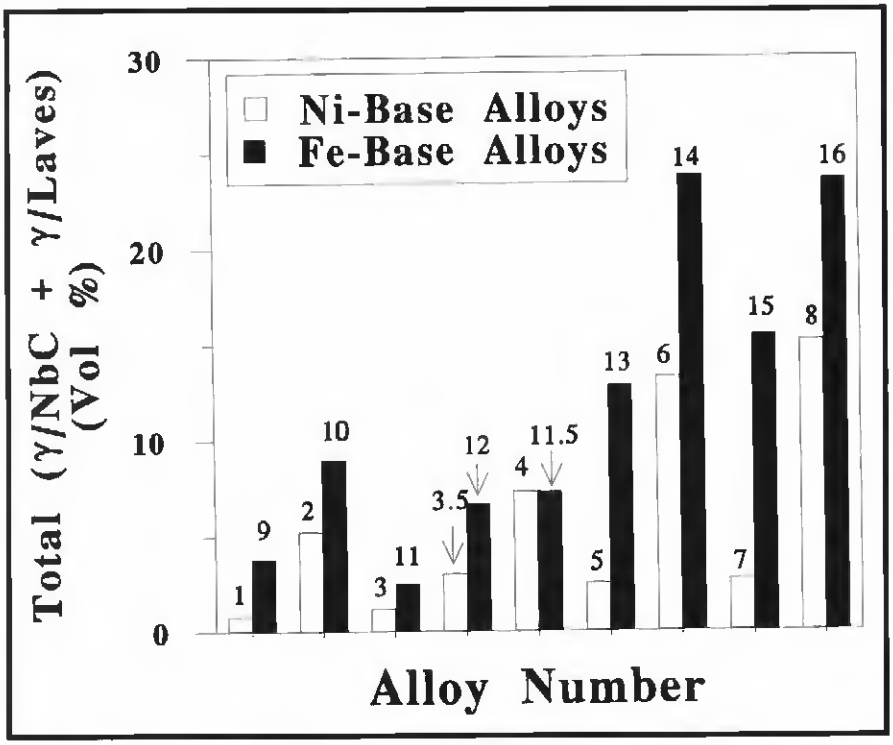

Fig. 3 — Quantitative image analysis results showing amount of total eutectic-type constituents.

MCL is generally saturated at the 2.5% strain level. At these strain levels, it is normally expected that cracking will span a major fraction of, if not the entire, length of the mushy zone.

Microstructural Characterization

Light optical microscopy (LOM) was conducted on Varestraint and DTA samples polished through 0.04-pm colloidal silica and electrolytically etched in a 10% chromic acid + 90% water solution at 3 V. Scanning electron microscopy was conducted on weld metals (prepared using the same procedure) using a JEOL 6300 field emission gun scanning electron microscope (FEG-SEM) at an accelerating voltage of 15 kV. The Varestraint samples were mounted in thermal setting epoxy to provide a planar view of the solidification cracks that intersected the specimen surface. After mounting, the surfaces were lightly ground with 600-grit SiC paper to remove a very thin layer of surface material and provide a flat area in the crack region for subsequent polishing and etching. Quantitative image analysis (QIA) was conducted on autogenous GTA welds at locations far removed from solidification cracks. Area fractions of total eutectic-type contents and, where possible, individual γ/NbC and γ/Laves eutectic-type constituents were measured along the centerline of each weld with at least ten SEM photomicrographs. Area fractions were assumed to be equivalent to volume fractions. Electron probe microanalysis (EPMA-WD5) was conducted on a JEOL 733 probe at an accelerating voltage of 15 kV and beam current of 20 nA. All EPMA samples were mounted in thermal setting epoxy, polished flat to a 0.3-μm finish using an alumina slurry, ultrasonically cleaned in acetone and carbon coated prior to analysis. The K_α lines were used for Fe, Ni, Cr and Si, while the L_α line was used for Nb. Raw data were reduced to weight percentages using a ZAF algorithm.

Results and Discussion

Solidification

The solidification behavior of these alloys has been described through microstructual analysis (Ref. 16) and solidification modeling (Ref. 17) in separate articles. The important features are summarized below as they provide a necessary framework for detailed interpretations of the weldability results. Typical DTA cooling scans for Alloys 2 and 16, which represent the two types of reaction sequences observed among the experimental alloys, are presented in Fig. 1.

The corresponding microstructures of GTA welds and DTA samples are presented in Fig. 2. The first type of solidification sequence, which was observed for all alloys except 2, 3.5 and 4, can be described by a three-step process: 1) Primary $L \rightarrow \gamma$ solidification in which the interdendritic liquid becomes enriched in Nb and C; followed by 2) a eutectic-type $L \rightarrow (\gamma+NbC)$ reaction, which depletes the interdendritic liquid of C; and 3) termination of solidification by a second eutectic-type reaction $L \rightarrow (\gamma + Laves)$. The broad peak associated with the $L \rightarrow (\gamma + NbC)$ reaction indicates this transformation occurs over a wide temperature range, while the narrow peak associated with the $L \rightarrow (\gamma + Laves)$ reaction indicates this step occurs over a small temperature interval (Ref. 16). Identification of the NbC and Laves phases shown in Fig. 2 was confirmed through EPMA measurements on coarse phases in DTA samples and backscattered electron kikuchi patterns collected from finer phases in weld metal samples (Refs. 16, 21). The Ni-based alloys with high C/low Nb (Alloys 2, 3.5 and 4) represent the only exception to this general solidification sequence. These alloys did not show any exothermic peaks after the $L \rightarrow (\gamma + NbC)$ reaction and did not exhibit any of the Laves phase in the as-solidified microstructure. This indicates that solidification terminated with the $L \rightarrow (\gamma + NbC)$ reaction. The amounts of total eutectic-type constituents (γ/NbC + γ/Laves) and, where possible, individual γ/NbC and γ/Laves constituents, are summarized in Figs. 3 and 4. The data are arranged to permit comparisons among Ni-based and Fe-based alloys with similar levels of solute elements (Nb, Si, and C).

As discussed in detail later, the solidification cracking resistance of these alloys is controlled, to a large degree, by the relative amounts of γ/NbC and γ/Laves constituents. Thus, it is instructive to consider the relation between alloy composition and relative phase fractions of γ/NbC and γ/Laves displayed in Figs. 3 and 4. At similar levels of minor alloy additions (Nb, Si and C), the iron-based alloys generally form higher levels of total eutectic-type constituents. Measurements of the individual eutectic-type constituents (Fig. 4) indicate that this response can be attributed primarily to the formation of higher amounts of γ/Laves in the Fe-based alloys. The addition of Fe to Nb-bearing Ni-based alloys is well known to stabilize the Laves phase (Ref. 22). Thus, Fe additions to the austenite matrix, at the expense of Ni, can be expected to promote the formation of more γ/Laves, as observed here. The addition of Si has a similar effect, as the amount of γ/Laves always increases with increasing Si within a given matrix composition (in Fig. 3, compare Alloys 5 to 7, 6 to 8, 13 to 15 and 14 to 16). The Laves promoting tendency of Si has also been documented in superalloys (Ref. 23). Niobium additions promote higher amounts of total eutectic. This is to be expected, since each of the secondary phases that form in the eutectic-type structures (NbC and Laves) are both highly enriched in Nb. At high C levels, Nb additions generally promote more γ/NbC (compare Alloys 2 to 6, 4 to 8, 10 to 14, 11.5 to 16). When the C and Fe levels are both high, Nb additions will increase the amounts of both the γ/NbC and γ/Laves constituents (compare Alloys 10 to 14 and 11.5 to 16). Alloys with high C levels (even-numbered alloys) form large amounts of the γ/NbC eutectic-type constituent. The presence of NbC and Laves has been observed in a large number of commercial superalloys, including Alloys IN625 (Ref. 12), IN718 (Ref. 8), IN909 (Ref. 24), IN903 (Ref. 23), IN519 (Ref. 11), Thermo-Span (Ref. 26) and IN625 weld cladding (Refs. 10, 27). The experimental alloys used in this work properly simulate the wide range of microstructures formed in commercial superalloys and weld cladding.

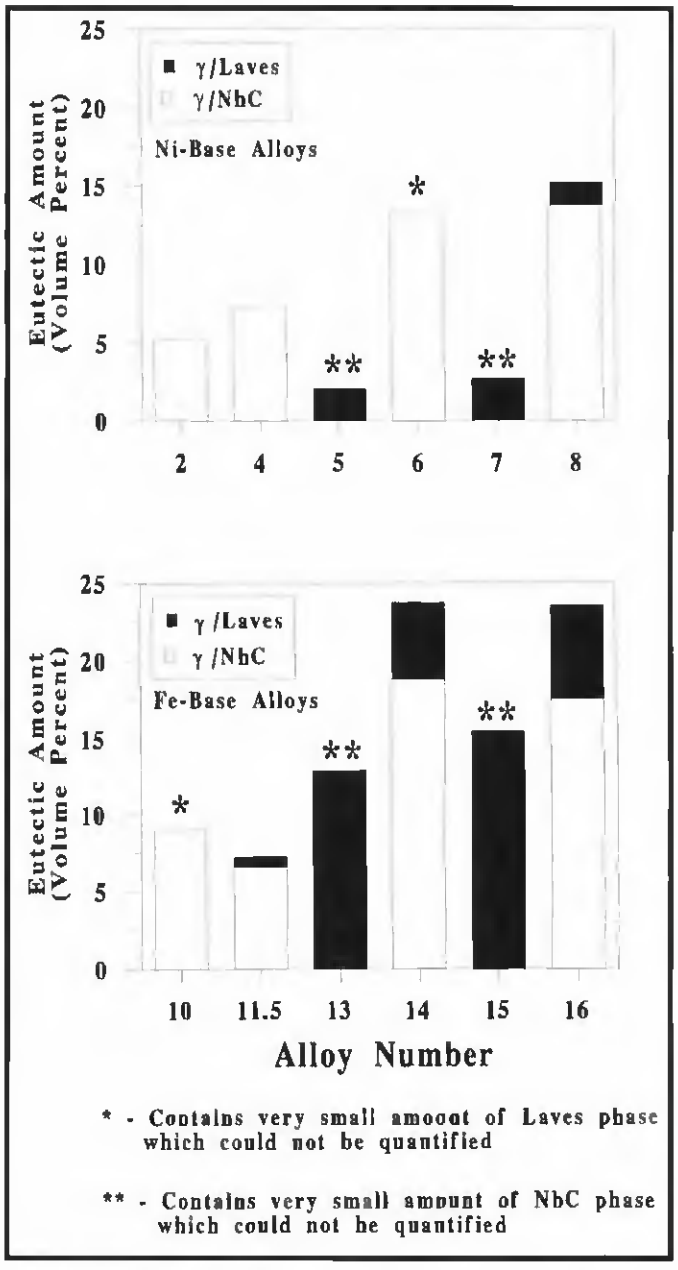

Fig. 4 — Quantitative image analysis results showing amount and individual γ/NbC and γ/Laves constituents.

The solidification reactions in these experimental multicomponent alloys and commercial alloys are similar to those expected in the pure ternary Ni-Nb-C system (Refs. 28, 29). The liquidus projection for this system is shown in Fig. 5. The liquidus projection exhibits three primary phase fields that are of interest here, γ, NbC and Ni_3Nb. A primary C (graphite) phase field exists at high C contents, which is not of importance. As noted earlier, additions of Fe, Cr and Si to the Ni-Nb system are known to promote Laves at the expense of Ni_3Nb in commercial superalloys, as well as the experimental alloys utilized in this work. Thus, by replacing Ni_3Nb with Laves, the Ni-Nb-C liquidus projection can be utilized as a guide in developing a description of the solidification reactions in these alloys (Ref. 29).

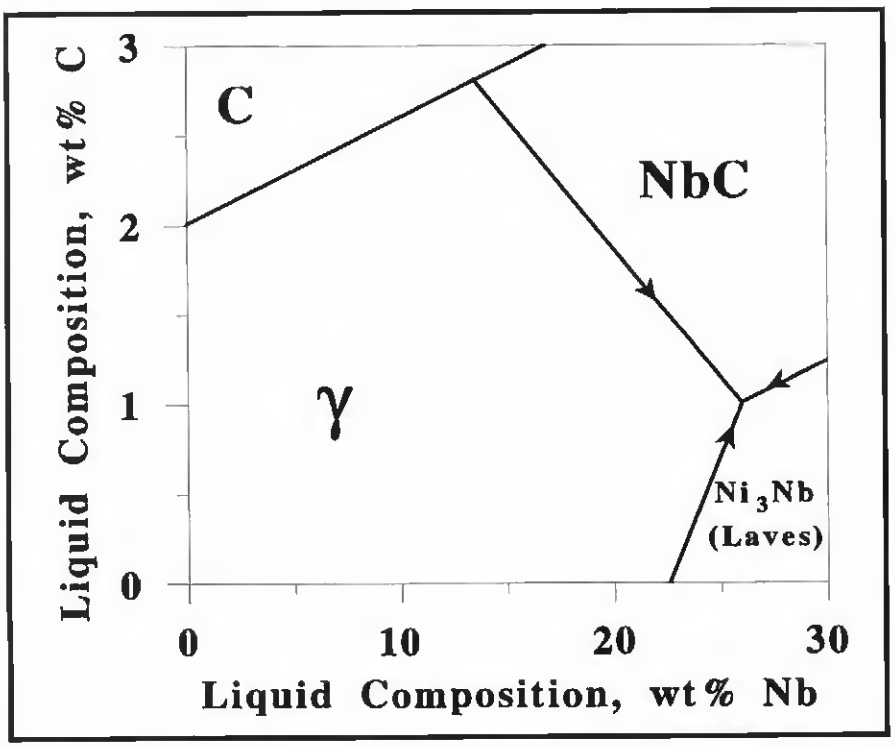

Fig. 5 — Liquidus projection for the Ni-Nb-C system.

Solidification begins with formation of primary γ dendrites, which, upon forming, reject Nb and C to the liquid (Ref. 16). As solidification proceeds, the liquid composition moves away from the Ni corner, becoming progressively richer in Nb and C until the line of two fold saturation between γ and NbC is reached. At this point, the maximum solubility of Nb and C in the austenite matrix is exceeded and the γ and NbC phases form simultaneously from the liquid by a eutectic-type reaction as the liquid composition travels down the line of twofold saturation. Due to its high C content, the formation of NbC depletes the liquid of C while the Nb content of the liquid continues to increase. For Alloys 2, 3.5 and 4, solidification is completed along the line of twofold saturation between γ and NbC, as no Laves phase was observed in these alloys. The initial reaction sequence is similar for the remaining alloys, except that solidification does not terminate with the L → (γ + NbC) reaction. Instead, the liquid composition continues to travel down the line of twofold saturation between γ and NbC, becoming progressively enriched in Nb (and depleted in C). According to the proposed Ni-Nb-C liquidus projection, solidification should terminate with the ternary L → (γ + NbC + Laves) reaction where the liquidus surface is at a minimum. Under this condition, the Laves and ternary γ and NbC phases should be intermixed in the final microstructure. However, this type of structure is not observed in any of the alloys that form both the NbC and Laves phases (*e.g.*, Fig. 2). Instead, the γ/NbC and γ/Laves eutectic-type constituents are always distinctly separated. This suggests that the liquidus projection for the alloys in this work is more properly represented by a class II reaction (Ref. 30). In this case, the local minimum on the liquidus surface occurs where the line of twofold saturation separating the γ and Laves phases intersects the Ni-Nb side of the diagram. The solidification sequence for alloys with this type of surface would occur as follows. After primary γ solidification, the liquid composition travels along the line of twofold saturation separating the γ and NbC phases during the L → (γ + NbC) reaction. This process continues until the class II reaction is reached, at which point the NbC stops forming as the L → (γ + NbC) reaction is replaced by the L → (γ + Laves) reaction. Solidification is completed at the Ni-Nb side of the diagram by the L → (γ + Laves) reaction. This solidification sequence accounts for the two spatially separate γ/NbC and γ/Laves eutectic-type constituents, which are observed experimentally.

The qualitative description of solidification discussed above has been described in a quantitative sense in separate articles (Refs. 16, 17). In that work, the position of the boundaries separating the γ, NbC and Laves phase fields for these experimental alloys was determined through EPMA measurements. The multicomponent alloys were modeled as a ternary system by grouping together the Fe, Ni and Cr matrix elements to form the γ "component" of the γ-Nb-C system. Solute redistribution of Nb and C between the liquid and solid phases was modeled using a previous approach developed by Mehrabian and Flemings (Ref. 31), with modifications made to account for the high diffusion rate of C in the solid. Values for the equilibrium distribution coefficients of Nb and C, which are needed in the solute redistribution calculations, were determined through a combination of EPMA and DTA techniques. A summary of the modeling results, which are important for interpreting the weldability data, is shown in Fig. 6. Figure 6A shows the calculated primary solidification paths of Alloys 1 through 4 superimposed on the experimentally determined liquidus projection. Note that the nominal alloy composition is given by the start of the solidification path. The alloy number of each path is noted in the figure. The start temperatures of the L → (γ + NbC) reaction, which represents the intersection of the primary solidification path with the line of twofold saturation separating γ and NbC, are noted for several alloys. The start temperature for the L → (γ + Laves) reaction is also noted. These temperatures were determined through DTA.

The point of intersection between the primary solidification path and line of twofold saturation is a strong function of C content. Although C additions are intuitively expected to promote the γ/NbC eutectic-type constituent, this analysis provides a quantitative rationale for the observed behavior. As the nominal C content is increased, the interdendritic liquid becomes more highly enriched in C and the intersection point occurs at higher C contents. As a result, the liquid composition must "travel" a long distance down the L → (γ + NbC) line of twofold saturation, forming γ/NbC as it travels, before the γ/Laves constituent can possibly form. Carbon additions raise the start temperature of the L → (γ + NbC) reaction and induce a concomitant decrease in the temperature interval of the primary L → γ stage of solidification. As discussed in more detail below, this effect has important implications with regard to fusion zone solidification cracking response.

The effect of matrix composition is presented in Fig. 6B. Alloys 2 and 10 have very similar levels of solute content, but different matrix compositions (Alloy 2 is Ni-based while Alloy 10 is Fe-based).

The matrix composition has a strong influence on the segregation potential of Nb (Ref. 16) as measured through the equilibrium distribution coefficient, k_{Nb}. The value of k_{Nb} in the Ni-based alloys is equal to 0.46, while k_{Nb} in the Fe-based alloys is only 0.25 (Ref. 16). As k_{Nb} is reduced, Nb segregates more aggressively to the liquid. Thus, at any given level of C in the liquid, the Fe-based alloys will always possess more Nb. As a result, the Fe-based alloys will have more liquid remaining after primary solidification, and the Nb content in that remaining liquid will be higher. These effects from the reduced k_{Nb} value are the primary reasons for the higher amount of total eutectic-type constituents observed in the Fe-based alloys — Fig. 3. The validity of the solidification model was confirmed by comparing the calculated and measured amounts of γ/NbC and γ/Laves constituents in the experimental alloys, and reasonable agreement was found (Ref. 17).

Weldability

Effect of Solidification Temperature Range

Figure 7 shows the maximum crack length (MCL) of each alloy. (The alloy compositions are summarized in Table 1). Within the Ni-based alloys, there is a clear separation in weldability among the low-C alloys (≤0.017 wt-% C) with relatively poor weldability and the high-C alloys (≥0.052 wt-% C), which show very good resistance to solidification cracking. Within the Fe-based alloys, the addition of C is only beneficial when the Nb content is low (≤1.93 wt-%), and the C level must he above 0.10 wt-% to provide the advantageous effect. For example, Alloys 11.5 and 12 have essentially identical levels of all other elements except C (Alloy 12 has 0.079 wt-% C and Alloy 11.5 has 0.116 wt-% C). This small variation in C content leads to a substantial difference in the MCL values. Within the Fe-based alloys with high Nb (Alloys 13–16), C has no beneficial effect even at the 0.21 wt-% level.

MCL values for commercial alloys tested using identical Varestraint equipment, welding conditions, weld sizes and augmented strain are also plotted in Fig. 7. Previous work (Refs. 8, 20) has shown that the saturated strain for these alloys is <2.5% under these test conditions. Alloys IN718 and IN625 are Nb-bearing superalloys that have been shown to be fairly susceptible to solidification cracking (Refs. 7, 8). Other Nb-bearing alloys have shown this relatively high susceptibility as well (Refs. 11, 26). These commercial alloys have C levels of ≈0.04 wt-%, which is intermediate to the experimental alloys utilized here. It is interesting to note that their MCL values fall within the range of the experimental alloys. This indicates that the experimental alloys accurately simulate the weldability behavior of comparable commercial superalloys. The low MCL value of 304 stainless steel is typical, as this alloy is known to exhibit excellent weldability. The high-C alloys show cracking resistance comparable to 304 stainless steel. This is a significant improvement over the

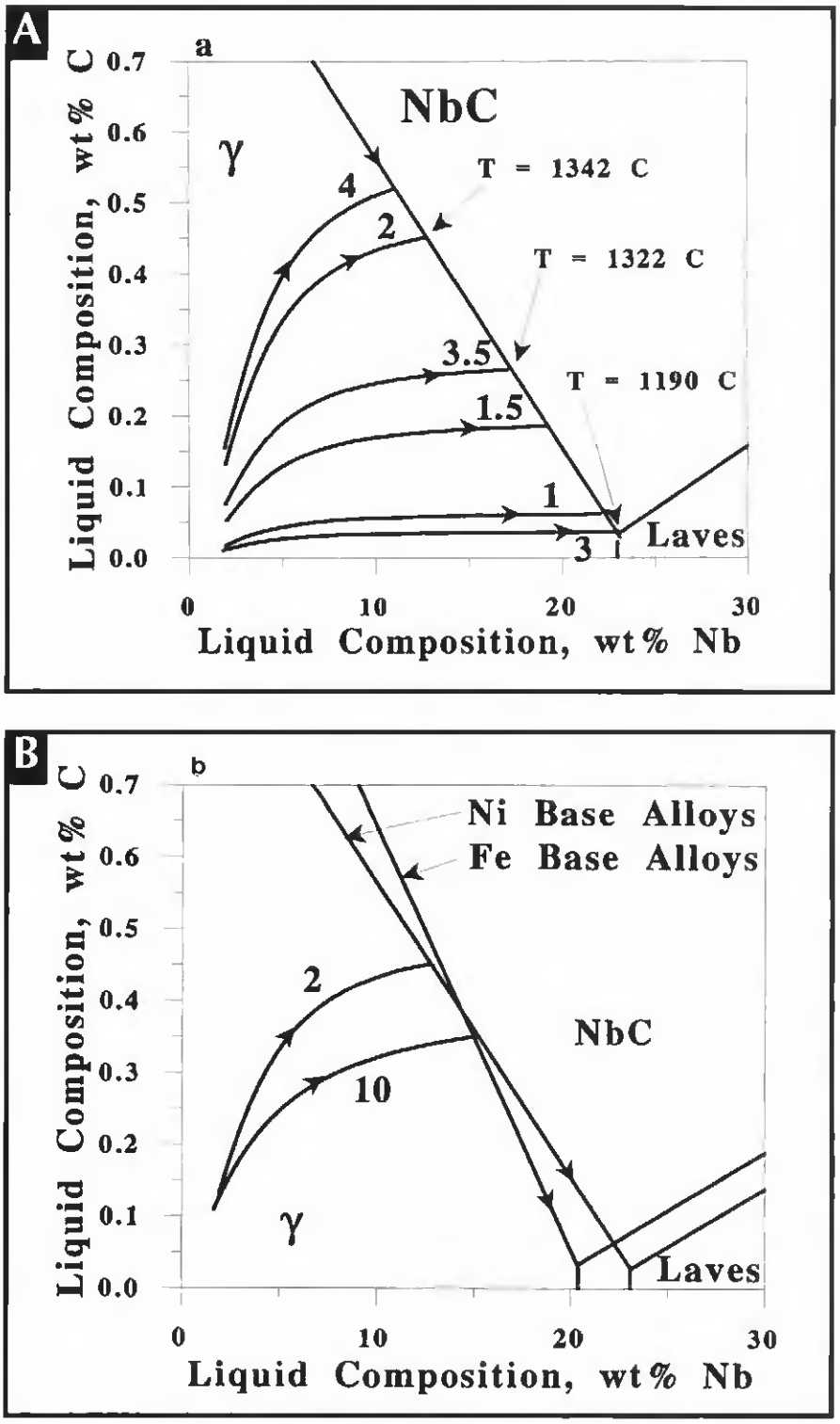

Fig. 6 — A — Calculated primary solidification paths of Alloys 1 through 4 superimposed on the experimentally determined liquidus projection; B — calculated primary solidification paths of Alloys 2 and 10 superimposed on the experimentally determined liquidus projection (Refs. 16, 17).

Table 2 — Summary of Reaction Temperatures and Solidification Temperature Ranges

Alloy	Liquidus Temperature (°C)	L → (γ + NbC) Temperature (°C)	L → (γ + Laves) Temperature (°C)	ΔT_s (°C)
2	1416.7 (1.2)	1341.5 (0.7)	NA	75.2
3	1412.3 (0.6)	ND	1190[a]	222.3
3.5	1410.5 (0.7)	1322.0 (1.4)	NA	88.5
4	1407.3 (0.6)	1330.0 (1.3)	NA	77.3
5	1391.0 (1.0)	ND	1190.0[a]	201.0
6	1390.0 (1.0)	1332.0 (1.4)	1190.0[a]	200.0
7	1387.7 (1.5)	ND	1190.0[a]	197.7
7.5	1382.0 (1.4)	1305.5 (0.7)	1190.0[a]	192.0
8	1379.3 (0.6)	1328.0 (2.8)	1190.0[a]	189.3
Ni-1	ND	ND	1190.0	NA
9	1430.4 (0.9)	ND	1249.3[b]	181.1
10	1426.1 (0.8)	1357.5 (0.7)	1249.3[b]	176.8
11	1423.9 (1.1)	ND	1249.3[b]	174.6
11.5	1419.6 (0.2)	1347.5 (2.1)	1249.3[b]	170.3
12	1418.8 (0.2)	1348.0 (1.4)	1249.3[b]	169.5
13	1401.1 (0.7)	1332.5 (0.7)	1249.5 (3.5)	151.6
14	1392.0 (0.3)	1360.8 (2.2)	1243.0 (2.1)	149.0
15	1392.6 (0.6)	1289.5 (0.8)	1256.3 (1.2)	136.3
16	1385.6 (0.3)	1355.2 (1.7)	1248.2 (4.8)	137.4

NA = Not applicable.
ND = Not detected.
(a) Estimated from sample Ni-1.
(b) Estimated from average of Fe base high Nb alloys.
Values in parenthesis are standard deviations calculated from at least three measurements.

Table 3 — γ/Laves Average Constituent Compositions

Alloy/Sample	Fe	Ni	Cr	Nb	Si
Alloy 7 DTA	4.9 ± 0.2	59.4 ± 0.8	10.2 ± 1.0	24.3 ± 0.7	1.7 ± 0.1
Alloy 7.5 DTA	4.9 ± 0.2	58.1 ± 1.7	11.4 ± 0.8	23.5 ± 1.3	2.0 ± 0.1
Alloy 8 DTA	4.4 ± 0.2	60.3 ± 0.5	11.3 ± 0.3	21.5 ± 0.5	2.5 ± 0.2
Ni-1 GTA melt	7.0 ± 0.1	52.2 ± 0.4	16.7 ± 0.2	23.1 ± 0.5	1.0 ± 0.1
Alloy 13 Weld	31.4 ± 1.8	29.8 ± 1.1	16.6 ± 0.6	21.1 ± 1.3	0.3 ± 0.1
Alloy 13 DTA	31.2 ± 0.9	30.4 ± 0.5	17.3 ± 0.2	20.9 ± 1.0	0.3 ± 0.1
Alloy 14 Weld	31.0 ± 1.1	29.5 ± 0.8	16.8 ± 0.7	22.4 ± 2.4	0.3 ± 0.1
Alloy 15 Weld	32.7 ± 0.5	29.7 ± 1.0	16.7 ± 0.4	20.1 ± 0.9	0.9 ± 0.1
Alloy 16 Weld	32.7 ± 0.4	30.8 ± 0.7	16.9 ± 0.1	18.3 ± 0.7	1.3 ± 0.1
Alloy 16 DTA	28.6 ± 1.9	33.4 ± 1.4	16.5 ± 0.9	19.8 ± 1.2	1.7 ± 0.1

All values in wt-%.

experimental and commercial alloys with low-to-moderate C contents.

As discussed in the section on solidification, C content has a significant effect on the primary solidification path and resultant solidification temperature range of these alloys. As the C content is increased, the primary solidification path is driven far into the C-rich side of the solidification surface and intersects the γ/NbC line of twofold saturation at relatively high temperatures near the end of solidification. Thus, C additions decrease the solidification temperature range of the primary L → γ reaction. Considering this effect, together with the general relation between cracking tendency and the solidification temperature range (ΔT_s), a correlation between MCL and ΔT_s might be expected. The solidification temperature range can be determined from DTA measurements. With respect to the upper limit of the solidification temperature range, the weld metal solidifies epitaxially from the base metal so there is no undercooling during solidification (Ref. 32) (*i.e.*, undercooling associated with nucleation of solid). Therefore, the upper limit of the solidification temperature range is well defined by DTA measurements of the on-heating liquidus. With respect to the lower limit of the solidification temperature range, previous work (Refs. 16, 17) showed that the type, quantity and composition of the terminal constituents were essentially identical for the DTA samples and GTA welds of the same bulk composition. Since these terminal constituents have the same composition in either case and one phase of the constituents (the austenite) can grow easily from the primary constituent, it is to be expected that the solidification temperature (range) of the terminal constituents will be similar irrespective of the cooling rate. Moreover, the modeling results from the previous work (Refs. 16, 17) showed that for the cooling rates in the DTA samples and the GTA welds, the partitioning of the two elements, which primarily affect the solidification temperature range (*i.e.*, Nb and C), is similar in both cases. Therefore, the DTA measurements of solidification temperature range provide a reasonable measure of the solidification temperature range for the GTA welds.

The liquidus temperature of each alloy is listed in Table 2 along with the temperatures of eutectic-type reactions, which occur during solidification. All samples, except Alloys 2, 3.5 and 4, exhibited the γ/Laves eutectic-type constituent. Thus, the temperature of the L → (γ + Laves) reaction should be utilized as the value for the terminal solidus temperature for all alloys except 2, 3.5 and 4. For the Ni-based alloys, the γ/Laves constituent formed in very small amounts, which precluded measurement of the L → (γ + Laves) reaction temperature by DTA. Thus, the temperature for this reaction was estimated from Alloy Ni-1, which formed a large amount of the γ/Laves constituent and produced a large exothermic DTA peak associated with the L → (γ + Laves) reaction. As shown by typical EPMA measurements in Table 3, the γ/Laves constituent in Alloy Ni-1 exhibited a composition similar to that observed in the Ni-based alloys. Thus, the reaction temperature measured for Alloy Ni-1 should serve as a good estimate for the terminal solidus temperatures of the

Ni-based alloys, which complete solidification by the L → (γ + Laves) reaction. The L → (γ + Laves) reaction temperature could not be directly measured in the Fe-based alloys with low Nb. The values measured in the high Nb iron-based alloys exhibit a fairly narrow range of 13°C. Thus, the average of these values should provide a good estimate for the low-Nb alloys. For Alloys 2, 3.5 and 4, the terminal solidus is taken as the value measured for the L → (γ + NbC) reaction as no γ/Laves constituent was observed. Positive identification of secondary phases could not be made in Alloy 1 or 1.5, so no solidification temperature range is reported for these alloys.

The γ/Laves composition measured by EMPA defines the composition of the liquid at the L → (γ + Laves) reaction (*i.e.*, the eutectic composition) (Refs. 8, 21). Note that the amount of Nb required in the liquid to start the L → (γ + Laves) reaction is lower in the Fe-based alloys. (Average Nb content is 23.1 wt-% in the Ni-based alloys and 20.4 wt-% in the Fe-based alloys). Thus, the L → (γ + Laves) reaction will start forming earlier in the solidification process with the Fe-based alloys and lead to a higher amount of the γ/Laves constituent. This effect, together with the reduced value k_{Nb}, in the Fe-based alloys, accounts for the higher amount of γ/Laves observed in the Fe-based alloys.

Figure 8 plots the MCL as a function of the solidification temperature range, and no correlation is readily apparent. Many alloys exhibit a rather wide solidification temperature range but show good weldability (low MCL). It should be emphasized that Cieslak (Ref. 7) was also unable to obtain a correlation between MCL and ΔT_s in his previous weldability reports on alloy IN625. This lack of correlation between MCL and ΔT_s suggests that crack propagation is being affected by the amount and distribution of solid and liquid phases within the mushy zone. Such potential effects can be assessed by conducting detailed microstructural characterization of the eutectic-type constituents in the vicinity of solidification cracks. These constituents transform from the terminal liquid, which existed in the grain boundary and interdendritic regions just before solidification is complete. Thus, the amount and morphology of these constituents provides a basis for developing an understanding of the distribution of solid and liquid phases within the mushy zone.

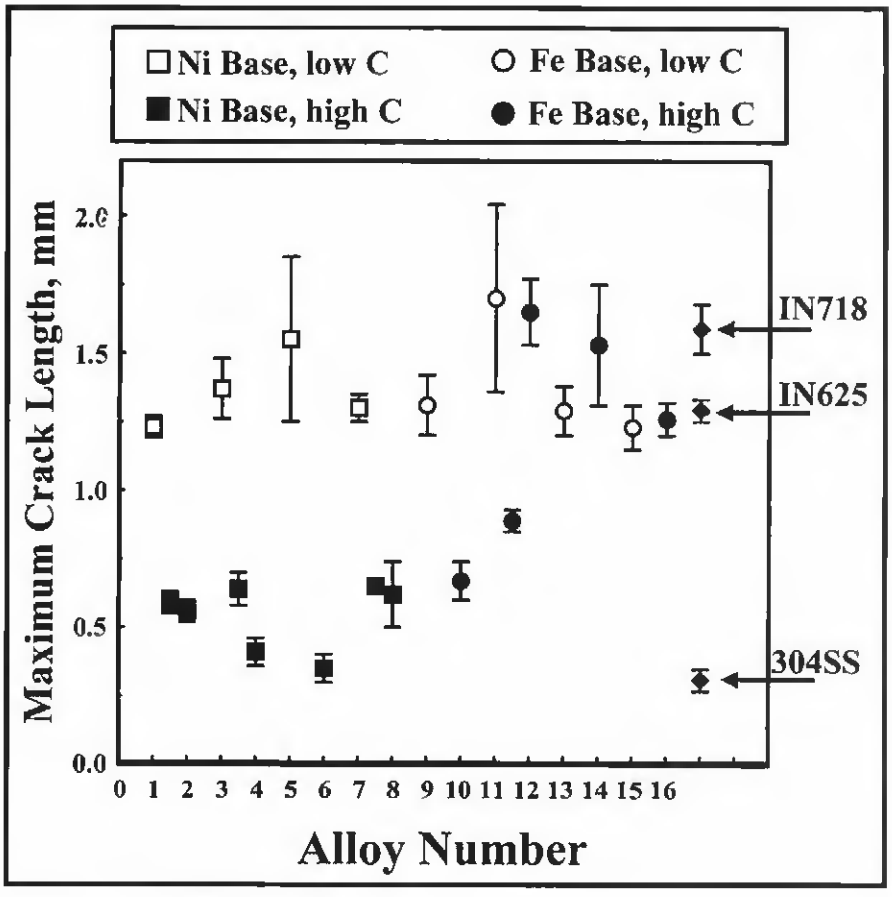

Fig. 7 — Maximum crack length of each alloy.

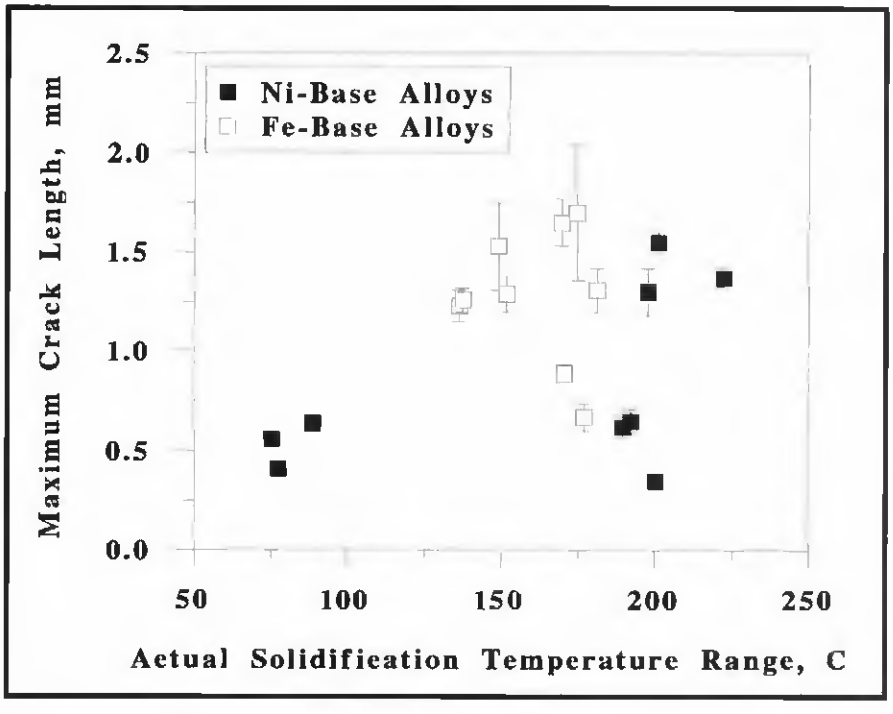

Fig. 8 — Maximum crack length as a function of the actual solidification temperature range.

Table 4 — Summary of Morphological Classification Schemes

Microstructure Type	Alloys within Classification
Type I	2, 3.5, 4
Type II	6, 7.5, 8, 10, 11.5
Type III	12, 14, 16
Type IV	1, 3, 5, 7, 9, 11, 13, 15

of Varestraint samples with the solidification sequences already discussed, it is possible to extend this general solidification description to identify four individual types of microstructural morphologies and their effect on cracking susceptibility. This proposed classification scheme sheds light on a more appropriate relation between MCL and ΔT_s, which could not be resolved by the initial plot in Fig. 8. All of the alloys can be grouped into one of four morphological classification schemes, and Table 4 lists the classification scheme that applies to each alloy.

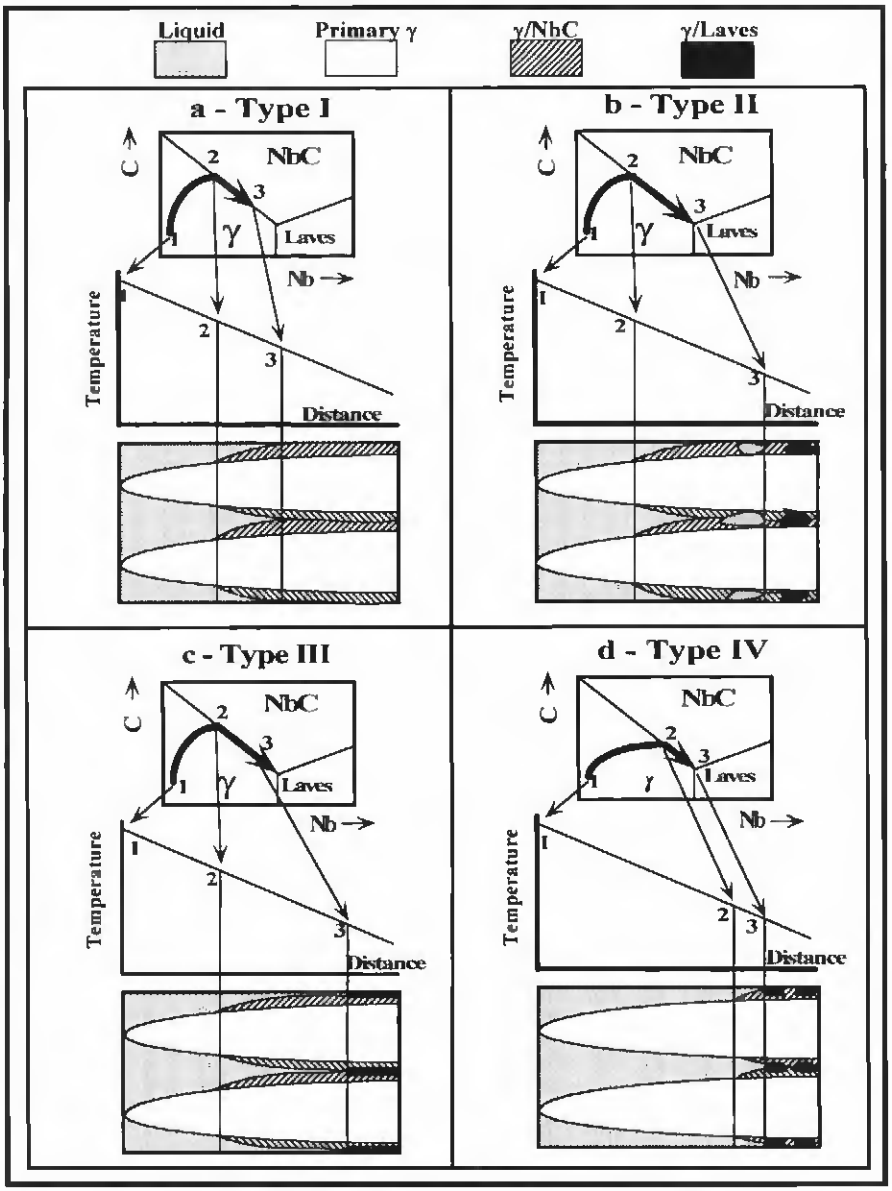

Fig. 9 — Schematic illustration showing development of various microstructural morphologies. A — Type I; B — Type II; C — Type III; D — Type IV.

Microstructural Evolution and Solidification Cracking

The general solidification process of these alloys was described in the solidification section above. By combining the microstructural characterization results

The development of each microstructural morphology is described schematically in Fig. 9. At the bottom of each figure, the formation of two neighboring dendrites within a grain are depicted growing into the trailing edge of the weld pool. The relation between temperature and phase stability in the mushy zone is shown by the temperature gradient diagram in the middle of the figure, where the dendrite tips are at the liquidus temperature. This point, given by zero distance behind the pool, represents the boundary between the liquid weld pool and solid + liquid mushy zone. The distance at which the actual temperature in the mushy zone reaches the terminal solidus temperature defines the boundary between the mushy zone and fully solidified weld metal. The relation between temperature, distance, phase stability and the solidification path is given by combining the γ-Nb-C liquidus surface with the other two figures. It is important to emphasize that the schematic illustrations presented in Fig. 9 are not intended to represent all of the details to microstructural evolution in the mushy zone nor are they intended to imply that single primary dendrite arms traverse the entire mushy zone. Rather, they are intended to pictorially describe the sequence of solidification events and the general distribution of microstructural constituents as they affect cracking susceptibility.

The Type I microstructure that develops during solidification cracking (Fig. 9A) is found in the Ni-based alloys with low Nb and high C that exhibit only the L → (γ + NbC) reaction (*i.e.*, Alloys 2, 3.5 and 4). A typical SEM photomicrograph from this group is presented in Fig. 10. At Step 1, the dendrite tips form from liquid of nominal composition as the actual temperature intersects the liquidus temperature (assuming negligible tip undercooling). Due to the high C/Nb ratio of these alloys, the interdendritic liquid then becomes highly enriched in C as the solidification path progresses toward the line of twofold saturation between γ and NbC. At Step 2, the primary solidification path intersects the line of twofold saturation at a relatively high temperature. As a result, the γ/NbC starts forming at a short distance from the dendrite tips. In other words, the primary L → γ solidification process is complete within a relatively small distance behind the advancing weld pool. There is a moderate amount of liquid present at Step 2. This is directly evident from the measured amount of the γ/NbC constituent, which is in the range of 3.0 to 7.3 vol-%, for this class of alloys. Because of the nature of solute redistribution (particularly carbon) in these alloys, the remaining liquid is completely consumed along the line of twofold saturation, so the γ/Laves constituent does not form (Ref. 17). From this description, it is

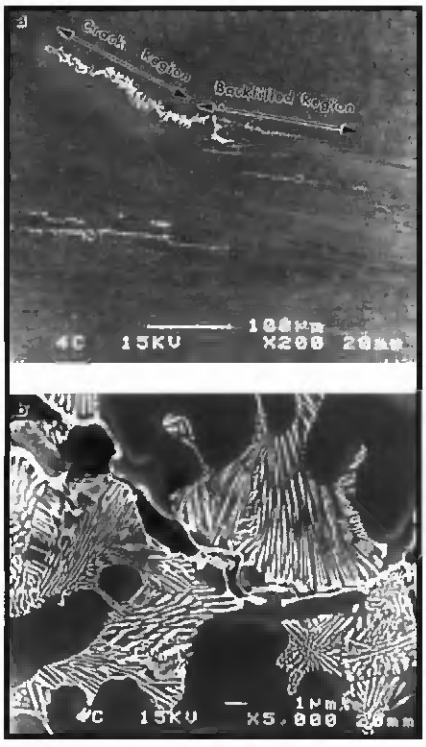

Fig. 10 — SEM photomicrograph showing the Type I microstructural morphology in the solidification crack of Alloy 4.

apparent that the mushy zone in these alloys is expected to be relatively small. Thus, the distance available for crack propagation is also relatively small, and this provides a major contribution to the excellent weldability observed experimentally.

In addition to the small mushy zone, the microstructures of Alloy 2 and 4 exhibit moderate amounts of the γ/NbC eutectic-type constituent that often backfills a portion of the crack — Fig. 10. A smaller amount of γ/NbC was observed in the solidification cracks in Alloy 1.5. The level of liquid needed for backfilling has been reported to be in the range of 6–10 vol-% (Refs. 4, 5), which is very close to the amount of terminal liquid present in Alloys 2 and 4 (5.2 ±1.5 and 7.3 ±1.3). Thus, when strain is imposed on the mushy zone of these alloys, a crack can only propagate a small distance and the leading edge of the crack is healed by backfilling. This description accounts for the small MCL values, moderate amounts of γ/NbC observed within the solidification crack and lack of the γ/Laves constituent.

Development of the Type II microstructure is shown schematically in Fig. 9B. This morphology is observed in the high Nb/high C nickel-based alloys and low Nb/high C iron-based alloys. The solidification process is similar to Type I, except that a larger amount of liquid is generally present at Step 2, which is not completely consumed during the L → (γ + NbC) reaction. As a result, the class II reaction point is reached and the γ/Laves constituent forms. A typical SEM photomicrograph showing the γ/NbC and γ/Laves morphology in the hot crack region for this class of alloys is shown in Fig. 11. This morphology was observed within the solidification cracks in all the Type II alloys. Reference to Table 2 shows that the L → (γ + Laves) reaction occurs at very low temperatures. Thus, the presence of liquid at the γ/Laves composition will extend the mushy zone out to larger distances. This has the potential of increasing the maximum crack length. However, the amount of γ/Laves constituent that forms in alloys of this group is below 2.3 vol-%. At this level, the γ/NbC always envelops the γ/Laves and keeps it isolated — Fig. 11. This suggests that the last residual liquid, from which

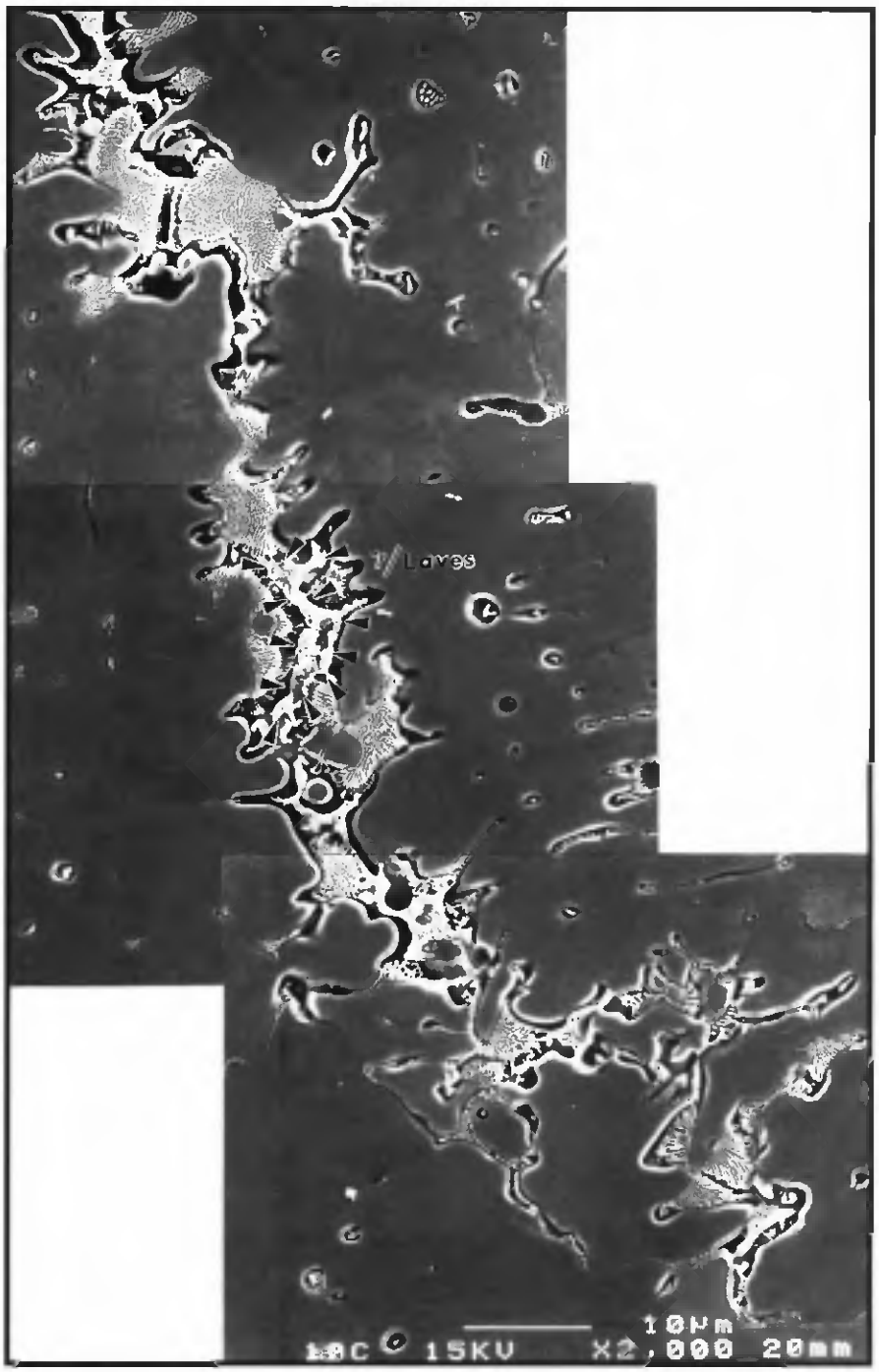

Fig. 11 — SEM photomicrograph showing the γ/NbC and γ/Laves morphology in the solidification crack of Alloy 10, Type II microstructure.

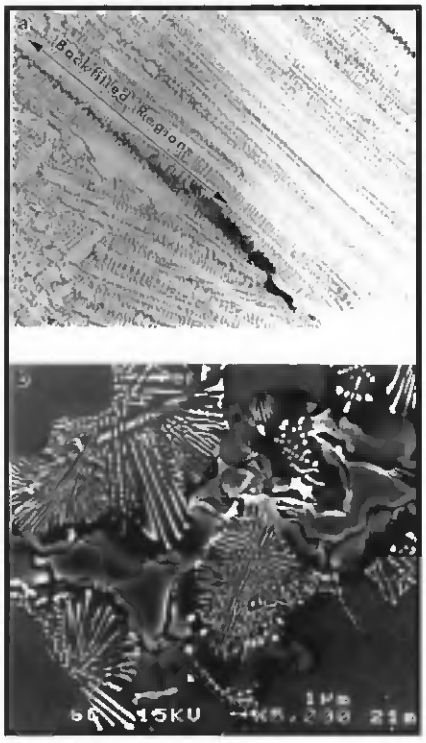

Fig. 12 — A — Low magnification LOM photomicrograph of backfilling in Alloy 6; B — higher magnification SEM photomicrograph showing solidification constituents in the same crack.

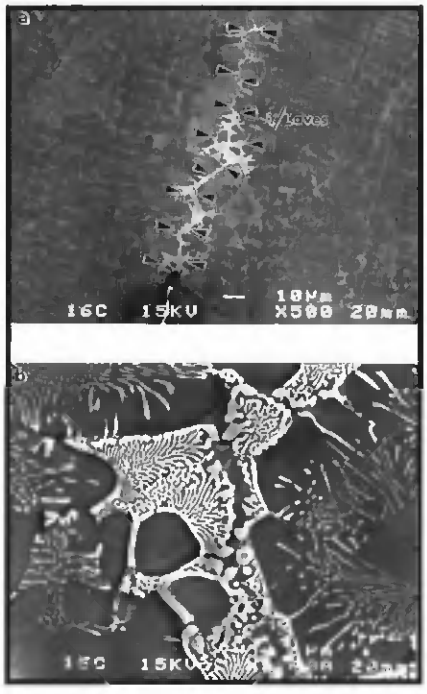

Fig. 13 — SEM photomicrograph showing the γ/NbC and γ/Laves morphology in the solidification crack of Alloy 16, Type III microstructure.

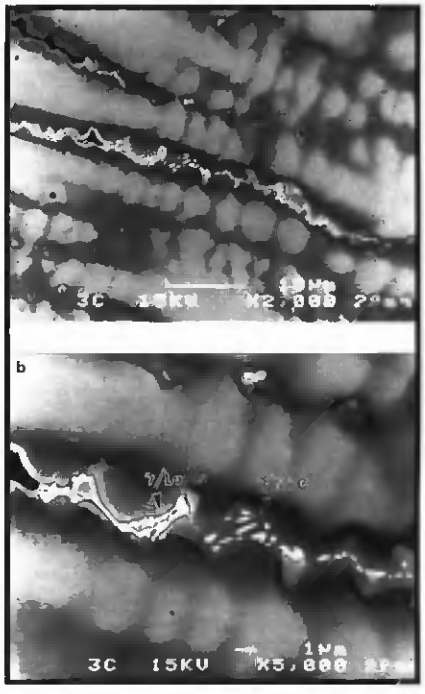

Fig. 14 — SEM photomicrograph showing the microstructural morphology in the solidification crack of Alloy 3, Type IV microstructure.

the γ/Laves forms, is also isolated within the mushy zone during crack advancement. With this type of morphology, the isolated liquid pockets should have little or no deleterious effect and crack propagation through the entire mushy zone is therefore unlikely. The Varestraint data tend to support this. The MCL values for these alloys is in the range of 0.35 to 0.89 mm, which is similar to the range of 0.41 to 0.64 mm observed in the Type I alloys, which form no γ/Laves and have excellent weldability. This may account for the lack of correlation between ΔT_s and MCL in Fig. 8 and will be discussed in more detail later. Evidence of backfilling was clearly evident in these alloys as well, and an example of this is provided in Fig. 12. This is not surprising, considering that these alloys contain 7.3 to 15.2 vol-% of liquid at Step 2.

The amount of total eutectic-type constituent in the Type II alloys, which corresponds to the amount of liquid at Step 2, is always above 7.3 vol-%. It is interesting to note that two alloys that fit into this microstructure type (Alloys 7.5 and 11.5) have almost identical amounts of liquid at Step 2 as Alloy 4, yet Alloy 4 does not form the γ/Laves constituent. The ability for liquid to remain after the L → (γ + NbC) reaction, and subsequently transform to γ/Laves, depends not only on the amount of liquid at Step 2 but also on the relative position of Step 2 and the segregation potential of Nb during the L → (γ + NbC) reaction. For example, Alloy 7.5 and Alloy 4 have essentially identical amounts of liquid at Step 2 (7.5 vol-%). However, due to its lower C/Nb ratio, the primary solidification path of Alloy 7.5 intersects the γ/NbC twofold saturation line closer to the class II reaction point. Thus, the remaining liquid in Alloy 7.5 does not have to travel as far as that in Alloy 4 to satisfy the composition conditions for the L → (γ + Laves) reaction. Alloy 11.5 also has about 7.5 vol-% liquid at Step 2. In this case, the lower value of k_{Nb} in the Fe-based alloys (k_{Nb} = 0.25 in Fe-based alloys and k_{Nb} = 0.46 in the Ni-based alloys) causes Nb to segregate more aggressively to the liquid so that the γ/Laves composition can be reached in the liquid.

Formation of the Type III microstructure is shown in Fig. 9C. This morphology is observed in the iron-based Alloys 12, 14 and 16. The main difference between this morphology and that of Type II lies within the amount and distribution of the γ/Laves constituent, where the Type III alloys form γ/Laves in quantities greater than 2.3 vol-%. As a result, the γ/Laves is observed in a continuous network. An example of this microstructural morphology is shown in Fig. 13. The advantageous effect of C, which was observed in the Ni-based alloys with high Nb and high C, is lost in the Fe-based alloys with comparable composition. Again, this effect is attributed to the higher segregation potential of Nb and lower amount of Nb required in the liquid to initiate the L → (γ + Laves) reaction, both of which translate into larger amounts of terminal liquid that undergoes the L → (γ + Laves) reaction at relatively low temperature. The actual size of the mushy zone in these alloys is expected to be similar to that for the iron-based Alloys 10 and 11.5 since each type terminates solidification with the L → (γ + Laves) reaction. However, with the residual liquid existing in a continuous network until the terminal L → (γ + Laves) reaction is reached, crack propagation through most of the mushy zone is more favorable for alloys that possess the Type III microstructure. Thus, the solidification temperature range governing crack propagation in these alloys should be appropriately given by the entire solidification range measured through DTA. Note that the MCL values observed for these alloys (1.26 to 1.65 mm) are consistently higher than those observed in the Type II alloys (0.35 to 0.89 mm) where the terminal liquid is isolated. As with the other alloys that form a large amount of terminal eutectic liquid, evidence of backfilling is observed in this microstructure type. However, it is worth noting that at this applied stain level, the amount of backfilling is small compared

to the MCL for all of the four microstructure types. For example, as shown in Fig. 3, Alloy 16 has almost 25 vol-% of eutectic-type constituent (the highest amount among all the alloys), which is well beyond the values typically reported to result in backfilling (Refs. 4, 5). Although the alloy forms a large amount of terminal eutectic liquid, inspection of Fig. 13A shows that backfilling occurs over a distance of approximately 0.14 mm, which is small compared to the MCL value of 1.26 mm. In fact, this amount of backfilling is not statistically different than the amount of variation typically observed when conducting multiple Varestraint tests under identical testing conditions. Thus, the values reported can be taken as an accurate representation of the MCL for each alloy without having to make detailed corrections for backfilling.

Lastly, the evolution of Type IV microstructures are shown in Fig. 9D. All of the low-C alloys fit into this classification category. These alloys exhibit a primary solidification path that travels very close to the γ/Nb binary side of the solidification surface. The primary path barely intersects the line of twofold saturation between γ and NbC before solidification terminates with the L → (γ + Laves) reaction. The eutectic-type reactions in this region of the solidification surface occur at low temperatures. Thus, with this solidification path, the mushy zone is relatively large and consists mainly of liquid and primary γ with small amounts of γ/NbC and γ/Laves. The total amount of terminal liquid in these alloys is generally low, between 0.8 and 3.8 vol-%. The only exception to this is Alloys 13 and 15, which form relatively large amounts of γ/Laves (12.9 vol-%) in a continuous network. The MCL values of all these alloys are high (1.23 to 1.70 mm), suggesting that crack propagation through all or most of the mushy zone is likely. A typical example of this morphology is presented in Fig. 14.

Based on these considerations, the terminal solidus temperatures affecting solidification cracking for Type III and Type IV microstructures should be appropriately given by the temperature of the terminal L → (γ + Laves) reaction. However, assuming crack propagation is difficult through the isolated regions of residual liquid in the Type II microstructures, the temperature range affecting solidification cracking for these alloys would be more realistically represented by using the temperature of the L → (γ + NbC) reaction as the terminal solidus point. The MCL and ΔT_s data are replotted in Fig. 15 using this effective solidification temperature range, and the trend between cracking susceptibility and the solidification temperature range is now more apparent. The data are grouped into two distinct regions of the plot that separates the low- and high-C alloys. This improved correlation, although somewhat qualitative, serves to support the proposed mechanisms of crack propagation

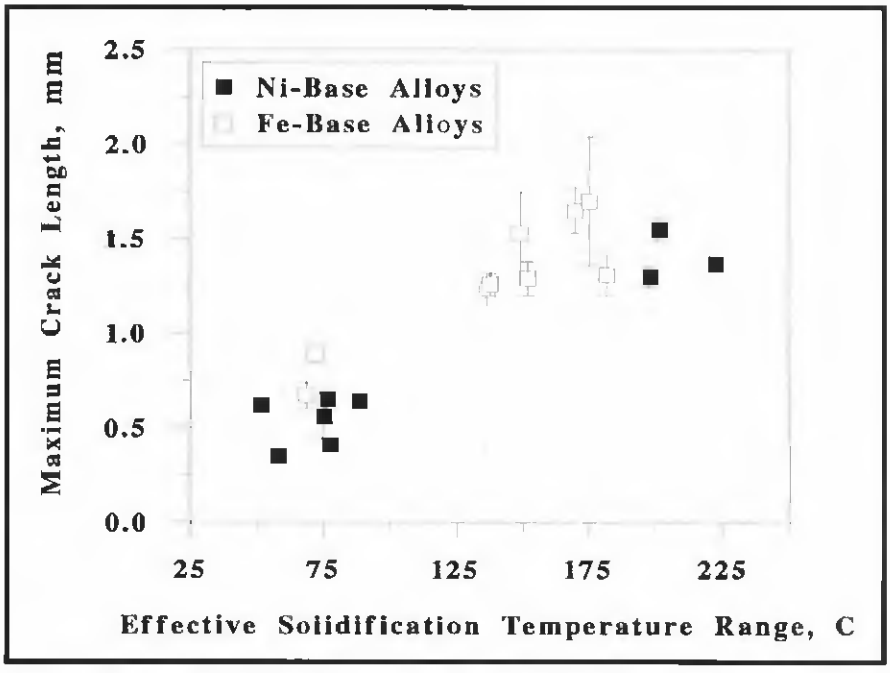

Fig. 15 — Replot of maximum crack length as a function of the effective solidification temperature range.

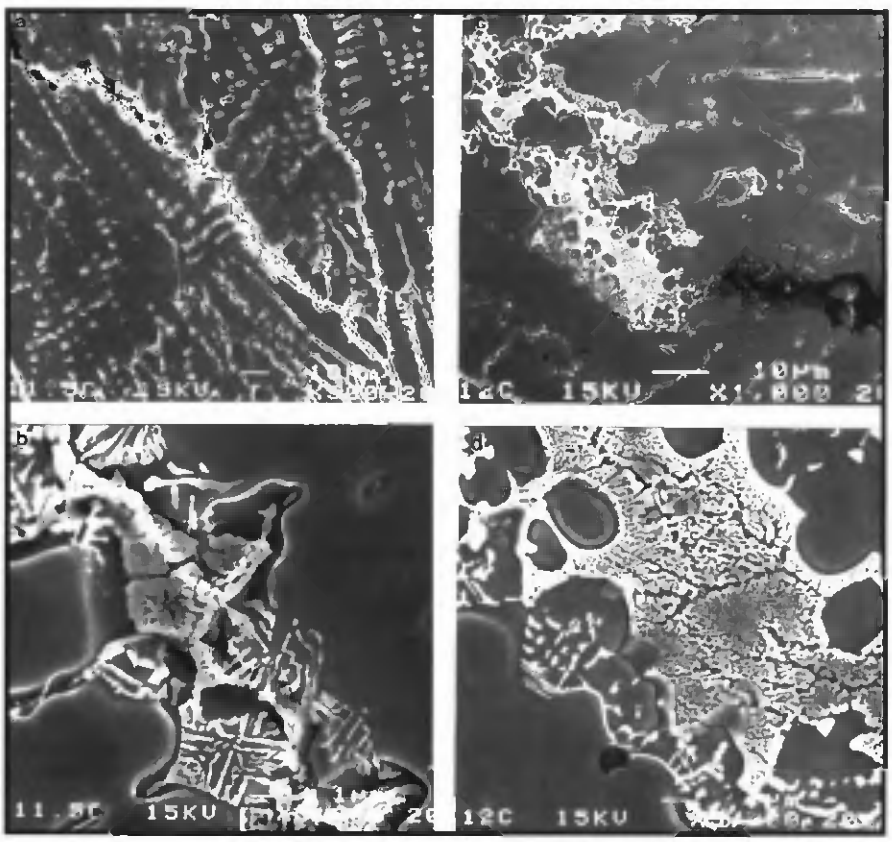

Fig. 16 — Comparison of microstructural morphologies in Alloys 11.5 (A and B) and Alloy 12 (C and D).

through the various types of microstructures. These results show that cracking susceptibility can be interpreted by knowledge of the solidification temperature range and type/amount of constituent that forms at the terminal stages of solidificaion. These factors are controlled by the solidification path as shown in Fig. 6 and schematically in Fig. 9. The solidification path is, in turn, governed by alloy composition. Thus, it is useful to conclude by summarizing the relations between these factors.

The addition of C is beneficial as it increases the start temperature of the L → (γ + NbC) reaction and reduces the temperature interval of the primary L → γ stage of solidification. This favors formation of Types I and II microstructures, which show very good weldability. This beneficial effect can be lost if more than approximately 2.3 vol-% of the γ/Laves constituent forms, at which point the Type III microstructure develops with a concomitant reduction in cracking resistance. The γ/Laves constituent is promoted by additions of Fe, Nb and Si. In the Ni-based alloys that have less than 11 wt-% Fe, the segregation potential of Nb is relatively low and the γ/Laves eutectic composition is relatively high. These two effects work together to reduce the amount of γ/Laves that forms, and C additions to the Ni-based alloys are consistently beneficial. Within the Ni-based alloys, the transition from Type I to Type II microstructures occurs when the Nb content is increased. The Type III microstructure does not form in the Ni-based alloys since the γ/Laves constituent is always below 2.3 vol-%.

When the Fe content is high, the segregation potential of Nb is increased and the γ/Laves eutectic composition is reduced. Thus, at equivalent levels of solute elements (Nb, Si and C), the Fe-based alloys will always form more γ/Laves than the Ni-based alloys — Fig. 4. As a result, the Fe-based alloys never form the Type I microstructure, and the Type II microstructure can only develop in the low-Nb alloys (Alloys 10 and 11.5). The sensitivity of microstructure type and resultant weldability to C content is reflected in the differences displayed by Alloys 11.5 and 12. Both have similar levels of Nb and Si, but Alloy 11.5 has slightly higher C (0.116 wt-% vs. 0.079 wt-%). At this level of Fe, Nb and Si, this small difference in C content is enough to induce a change in microstructure type. These two microstructural morphologies are compared in Fig. 16. When the Fe-based alloys have high Nb, a high amount of γ/Laves forms and leads to the Type III microstructure. Finally, for the low-carbon alloys, the solidification path always travels along the γ/Nb binary side of the liquidus surface and leads to the Type IV microstructure, which has relatively poor weldability. These relations were discussed qualitatively in this article. Results of solidification modeling presented in previous articles can be used to predict these interrelations in a quantitative sense (Refs. 16, 17).

Conclusions

The solidification and weldability of experimental Nb-bearing superalloys with systematic variations in Fe, Nb, Si and C were investigated by differential thermal analysis, Varestraint testing and microstructural characterization techniques. The following conclusions can be drawn from this work:

1) The general solidification sequence of these alloys can be described by a three-step process: 1) Primary L → γ solidification in which the interdendritic liquid becomes enriched in Nb and C; followed by 2) a eutectic-type L → (γ + NbC) reaction, which depletes the interdendritic liquid of C; and 3) termination of solidification by a second eutectic-type reaction L → (γ + Laves). This solidification reaction sequence is similar to that expected in the ternary Ni-Nb-C system and observed experimentally in many commercial alloy systems.

2) Carbon additions have a strong influence on the temperature interval of the primary L → γ stage of solidification. As the carbon content is increased, the L → (γ + NbC) reaction temperature increases and, as a result, reduces the temperature interval of the primary L → γ stage of solidification. In the Ni-based alloys, C additions above 0.052 wt-% significantly improve the solidification cracking resistance. Carbon additions to the Fe-based alloys are only advantageous when the Nb level is below 2 wt-%, and the C level must be above 0.12 wt-% for the beneficial effect to be observed.

3) There is generally no direct relation between the actual solidification temperature range and fusion zone cracking susceptibility of these experimental alloys, suggesting that crack propagation through the mushy zone is affected by the amount and morphology of solid and liquid phases in the mushy zone.

4) A classification scheme is proposed to provide a phenomenological explanation of the relation between the solidification temperature range, microstructural morphology and cracking propensity. This morphological description leads to an improved correlation between the (effective) solidification temperature range and fusion zone cracking tendency.

Acknowledgments

The authors extend their thanks to Dr. M. J. Cieslak at Sandia National Laboratories for useful discussions and review of the manuscript. One author (JND) gratefully acknowledges financial support for this research from the American Welding Society Fellowship Award. Preparation of the experimental alloys by B. Damkroger and M. Maguire at Sandia National Laboratory is also greatly appreciated. Sandia is a multiprogram laboratory operated by Sandia Corp., a Lockheed Martin company, for the United States Department of Energy under Contract DE-AC04-94AL85000.

References

1. Borland, J. C. 1960. Generalized theory of super-solidus cracking in welds (and castings). *British Welding Journal*, Vol. 7, pp. 508–512.

2. Zacharia, T. 1994. Dynamic stresses in weld metal hot cracking. *Welding Journal*, 73(7): 164-s to 172-s.

3. Brooks, J. A. 1993. On modeling weld solidification cracking. *Proceedings of Internal Conference on Modeling and Control of Joining Processes*, Orlando, Fla., pp. 174–185.

4. Clyne, T. W., and Kurz, W. 1982. The effect of melt composition on solidification cracking of steel, with particular reference to continuous casting. *Metall. Trans. B*, Vol. 13A, pp. 259–266.

5. Matsuda, F., Nakagawa, H., Katayama, S., and Arata., Y. 1982. Weld metal cracking and improvement of 25% Cr-20% Ni (AISI 310S) fully austenitic stainless steel. *Transactions of the Japan Welding Society*, Vol. 13, pp. 41–58.

6. Elmer, J. W. 1988. The influence of cooling rate on the microstructure of stainless steel alloys, Sc.D. thesis, Massachusetts Institute of Technology, Cambridge, Mass.

7. Cieslak, M. J. 1991. The welding and solidification metallurgy of Alloy 625. *Welding Journal* 70(2): 49-s to 56-s.

8. Knorovsky, G. A., Cieslak, M. J., Headley, T. J., Romig, A. D., and Hammetter, W. F. 1989. Inconel 718: A solidification diagram. *Metallurgical Transactions A*, Vol. 20A, pp. 2149–2158.

9. Clyne, T. W., and Davies, G. J. 1979. Comparison between experimental data and theoretical predictions relating to dependence of solidification cracking on composition. *TMA Proceedings of the International Conference on Solidification*, Sheffield, England, pp. 275–278.

10. DuPont, J. N. 1996. Solidification of an Alloy 625 weld overlay. *Metallurgical and Material Transactions A*, Vol. 27A, pp. 3612–3620.

11. Nakao, Y., Ohshige, H., Koga, S., Nishihara, H., and Sugitani, J. 1982. Effect of Nb/C on the sensitivity of liquation cracking in 24Cr-24Ni-1.5NbFe-base heat resisting alloy. *Journal of the Japan Welding Society*, Vol. 51, pp. 989–995.

12. Cieslak, M. J., Headley, T. J., Kollie, T., and Romig, A. D. 1988. A melting and solidi-

fication study of Alloy 625. *Metallurgical Transactions A*, Vol. 19A, pp. 2319–2331.

13. Robitz, E., and Edmonds, D. P. 1987. Abstracts of papers of 67th American Welding Society Meeting, pp. 136–138.

14. Patterson, R. A., and Milewski, J. O. 1985. GTA weld cracking — Alloy 624 to 304L. *Welding Journal* 64(8): 227-s to 231-s.

15. Cieslak, M. J., Hills, C. R., and Headley, T. J. 1986. *Microbeam Analysis*, A. D. Romig and W. F. Chalmers, eds., pp. 69–73.

16. DuPont, J. N., Robino, C. V., Marder, A. R., Notis, M. R., and Michael, J. R. 1997. Solidification of Nb-bearing superalloys, Part I. Reaction sequences. Accepted for publication in *Metallurgical and Material Transactions A*.

17. DuPont, J. N., Robino, C. V., and Marder, A. R. 1997. Solidification of Nb-bearing superalloys, Part II: Pseudo-ternary solidification surfaces. Accepted for publication in *Metallurgical and Material Transactions A*.

18. Savage, W. F., and Lundin, C. D. 1965. The Varestraint test. *Welding Journal* 44(10): 433-s to 442-s.

19. Savage, W. F., and Lundin, C. D. 1966. Application of the Varestraint technique to the study of weldability. *Welding Journal* 45(11): 497-s to 503-s.

20. Cieslak, M. J., Headley, T. J., and Frank, R. B. 1989. The welding metallurgy of custom age 625 PLUS alloy. *Welding Journal* 68(12): 473-s to 482-s.

21. DuPont, J. N. 1997. Solidification and Welding Metallurgy of Experimental Ni Base and Fe Base Alloys Containing Nb, Si, and C, Ph.D. thesis, Lehigh University, January, 1997.

22. Blazina, Z., and Trojko, R. 1986. *J. Less Common Metals*, Vol. 119, pp. 297–305.

23. Wlodek, S. T. 1963. *Trans. Am. Soc. Met.*, Vol. 56, pp. 287–303.

24. Cieslak, M. J., Headley, T. J., Knorovsky, G. A., Romig, A. D., and Kollie, T. 1990. A comparison of the solidification behavior of Incoloy 909 and Inconel 718. *Metall. Trans. A*, Vol. 21A, pp. 479-488.

25. Nakkalil, R., Richards, N. L., and Chaturvedi, M. C. 1993. Microstructural characterization of Incoloy 903 weldments. *Metall. Trans. A*, Vol. 24A, pp. 1169–1179.

26. Robino, C. V., Michael, J. R., and Cieslak, M. J. 1996. The solidification and welding metallurgy of Thermo-Span alloy. Accepted for publication in *Science and Technology of Welding and Joining*.

27. Zhao, Q. H., Gao, Y., Devletian, J. H., McCarthy, J. M., and Wood, W. E. 1992. Microstructural analysis of Ni alloy 625 cladding over carbon steel. *Proc. of 3rd Int. Conf. International Trends in Welding Science and Technology*. S. A. David and J. M. Vitek, eds., ASM, Materials Park, Ohio, pp. 339–343.

28. Stadelmajer, H. H., and Fiedler, M. L. 1975. The ternary system nickel-niobium-carbon. *Z. Metallkd.*, Vol. 66 (4): 224–225.

29. Radhakrishnan, B., and Thompson, R. G. 1989. Solidification of the nickel-base superalloy 718: a phase diagram approach. *Metall. Trans. A*, Vol. 20A, pp. 2866–2868.

30. Rhines, F. N. 1956. *Phase Diagrams in Metallurgy*, R. F. Mehl and M. B. Beaver, eds. McGraw Hill, New York, N.Y., pp. 175–185.

31. Mehrabian, R., and Flemings, M. C. 1970. Macrosegregation in ternary alloys. *Metallurgical Transactions A*, Vol. 1, pp. 455–464.

32. David, S. A., and Vitek, J. M. 1989. Correlation between solidification parameters and weld microstructures. *International Materials Review*, Vol. 34, pp. 213–245.

33. DuPont, J. N., Robino, C. V., and Marder, A. R. 1997. Modeling solute redistribution and microstructural development in fusion welds of Nb bearing superalloys. Accepted for publication in *Acta Materialia*.